



Article

A New Calibration Method for Broadband Complex Resistivity Measurement System of Rocks and Ores

Haojie Zhang ^{1,2}, Rujun Chen ^{1,2,*} , Shaoheng Chun ^{2,3,*} and Chao Xu ^{1,2}

¹ School of Geoscience and Info-Physics, Central South University, Changsha 410083, China; 225011090@csu.edu.cn (H.Z.); 225012135@csu.edu.cn (C.X.)

² AIoT Innovation and Entrepreneurship Education Center for Geology and Geophysics, Central South University, Changsha 410083, China

³ School of Integrated Circuits, Wuxi Institute of Technology, Wuxi 214121, China

* Correspondence: chrujun@csu.edu.cn (R.C.); chunsh123@126.com (S.C.); Tel.: +86-137-8708-0374 (R.C.); Tel.: +86-151-5064-8387 (S.C.)

Abstract: The complex resistivity (CR) measurement constitutes a practical methodology for investigating the internal structures of rocks and ores alongside their mineralogical compositions and the chemical properties of fluids. However, during complex resistivity testing, particularly at high frequencies, the leakage current caused by the distributed capacitance of the instrument's acquisition channels reduces the measurement accuracy. Additionally, the contact impedance of the measuring devices and the electromagnetic coupling effects of the measurement cables further affect the complex resistivity test results of samples. To accurately characterize samples' intrinsic induced polarization (IP) properties, we developed a broadband complex resistivity measurement system (1 mHz–100 kHz) for rocks and ores, comprising a complex resistivity analyzer and a sample holder, employing the four-electrode method. In this study, we establish a circuit model for the measurement system to analyze the influence of the distributed capacitance of the acquisition channels on the test results at elevated frequencies. We derive the error terms inherent in the instrument's measurements across various circuit design configurations and propose a novel method for calculating the distributed capacitance of the instrument's acquisition channels, the parasitic capacitance of the sampling resistor, and for calibrating data by reversing the polarity of the excitation signal. Furthermore, we investigate the effect of contact impedance within the measurement setup on test results and design two sample-testing devices. Through extensive testing on multiple circuit models and samples, the system achieves an accuracy of up to 1% within the 10 MΩ range. Its overall performance surpasses that of the Solartron 1260A impedance analyzer and traditional signal source forward connection calibration methods. This advancement holds significant implications for complex resistivity measurements and the study of rock physical properties.

Keywords: rock physics; spectral induced polarization; data acquisition and calibration; distributed capacitance; contact impedance



Academic Editor: Nikolaos Koukouzas

Received: 20 December 2024

Revised: 25 January 2025

Accepted: 27 January 2025

Published: 2 February 2025

Citation: Zhang, H.; Chen, R.; Chun, S.; Xu, C. A New Calibration Method for Broadband Complex Resistivity Measurement System of Rocks and Ores. *Appl. Sci.* **2025**, *15*, 1526.

<https://doi.org/10.3390/app15031526>

Copyright: © 2025 by the authors. Licensee MDPI, Basel, Switzerland. This article is an open access article distributed under the terms and conditions of the Creative Commons Attribution (CC BY) license (<https://creativecommons.org/licenses/by/4.0/>).

1. Introduction

The complex resistivity (CR) method, also known as spectral-induced polarization (SIP), is a geophysical technique used to describe the polarization characteristics of rocks. This is done by testing the impedance spectra of various samples under the influence of an external electric field [1]. Complex resistivity data consist of two components: the real part, which reflects the conductivity of charge flow within the sample, and the imaginary part,

which is associated with the accumulation of polarized charges on the internal and surface boundaries of the sample [2].

Due to the strong induced polarization (IP) effects of metallic ores under an external electric field, the CR method is commonly used in mineral exploration and development [3,4]. Typically, measurement frequencies for this method are below 1 kHz [3,5]. As measurement techniques and theoretical understanding have improved, the method has been widely applied in various fields. These include engineering geophysics [6,7], hydrogeological surveys [8,9], biomedical engineering [10], and plant disease and pest control [11,12]. Measurement frequencies have expanded from the traditional kHz range to hundreds of kHz.

Although the physical mechanisms behind CR-induced polarization are not fully understood, several theories have gained traction. Electrochemical polarization (or double-layer polarization) occurs at the interface between solid particles and pore fluids. This is attributed to reversible electrochemical diffusion processes, mainly at low frequencies [13–15]. Interfacial polarization (or Maxwell-Wagner polarization) dominates at higher frequencies. It describes the dielectric properties of rocks [2].

Despite the incomplete understanding of polarization mechanisms, observed polarization effects still reveal key relationships between the physical properties, material composition, and structural characteristics of samples. In some cases, these effects can be weak. For example, phase shifts in non-mineralized sedimentary samples may only be a few millivolts, which makes them difficult to detect with traditional measurement systems [16,17].

To capture the actual polarization characteristics of a sample, both the testing instrument and measurement apparatus must meet stringent requirements. At high frequencies (>1 kHz), studies have shown that the distributed capacitance in the instrument's acquisition channels can lead to significant phase errors [18–20]. Therefore, calibration of high-frequency data is essential before use. In addition to internal circuit design and material selection, the design of the measurement apparatus also plays a crucial role [21]. Polarization effects occur at low frequencies with measurement electrodes [22,23], electromagnetic coupling interference exists between measurement wires [24,25], and contact impedance from structural design [26] can affect measurement accuracy. Even when using the same apparatus for different sample types (e.g., rock samples vs. solutions), varying error responses can occur. This makes error analysis for the CR measurement system essential.

Given these testing challenges, increasing attention has been given to developing high-precision data calibration methods. Zimmermann et al. [27] designed an impedance analyzer and analyzed the effects of the instrument's acquisition channel distributed capacitance, and the material and positioning of the measurement electrodes on test data using sampling resistors below 1 k Ω . This led to accurate CR measurements across the mHz to kHz frequency range. Building on this work, Huisman et al. [28] improved calibration accuracy by using reverse current and potential electrodes to precisely estimate electrode impedance. Wang and Slater [29] developed an error estimation model using the error term $\omega C_{in} Z_x$ to approximate the impact of distributed capacitance in the acquisition channels. Furthermore, because of inevitable electromagnetic coupling in traditional four-electrode systems, Volkmann and Klitzsch [30] extended the frequency range to MHz by combining the four-electrode method (low frequency) with the two-electrode method (high frequency).

During field exploration, many researchers have focused on the arrangement and selection of electrode configurations. These approaches help suppress the apparatus effect under high-frequency conditions [26,31,32]. To extract effective induced polarization (IP) responses from measurement data, inversion models and methods can also be employed [33].

By leveraging differences in the transmission equations of the induced polarization field and the electromagnetic induction field, the two effects can be separated [32,34]. New measurement devices, methods, and electrodes have been continuously developed for use in high-precision CR measurement systems [22,34,35].

Currently, specialized instruments for measuring the complex resistivity of rocks and ores are not widely available. Most researchers rely on alternatives, such as impedance analyzers or LCR bridge instruments. These include the Solartron 1260A impedance analyzer from Solartron (Bognor Regis, UK) and the HP4194A impedance/gain-phase analyzer from Hewlett-Packard (Palo Alto, CA, USA). These instruments are primarily designed for measuring electronic components and typically use low-value sampling resistors ($<1\text{ k}\Omega$). Their calibration methods are based on the forward connection of signal sources and primarily account for the distributed capacitance of the acquisition channels. However, in testing high-impedance samples, which can have values up to $10\text{ M}\Omega$, using low-value sampling resistors leads to reduced voltage acquisition accuracy. Traditional calibration methods struggle to meet the precision requirements for such high-impedance samples.

To address the limitations in high-frequency complex resistivity measurement systems, this study introduces a novel measurement instrument designed for a resistance range of $50\ \Omega$ to $10\text{ M}\Omega$. A new calibration method is proposed, using both forward and reverse connections of the excitation signal source to calculate the distributed capacitance of internal acquisition channels, and the parasitic capacitance of sampling resistors, and to improve data calibration accuracy. The influence of contact impedance on measurement results is analyzed, and two sample testing devices are developed to extend the instrument's measurement range and improve its precision for high-impedance samples.

Through extensive testing with multiple circuit models and actual samples, the proposed system and calibration method achieve a measurement accuracy of 1% for resistances up to $10\text{ M}\Omega$. This performance surpasses that of the Solartron 1260A impedance analyzer and traditional calibration methods. The proposed system shows significant advantages for rock physical property measurements and spectral-induced polarization data processing.

2. Measurement System

2.1. System Overview

The calibration work in this study was conducted using a self-developed broadband electrical property measurement instrument for rocks and ores (CSUZA-FW08). Figure 1 presents the structural diagram of the measurement system. The instrument consists primarily of the execution unit, the measurement apparatus (sample holder), and an Android App. The measurements are performed using the four-electrode method, with a test frequency range covering one mHz to 100 kHz.

The central unit of the instrument, the execution unit, is the core of the measurement system. It consists of three main components: the signal source, acquisition system, and control system. The primary function of the execution unit is to receive control commands from the Android app, provide an integrated excitation source, perform core data acquisition, and transmit the data.

The low-power control system is based on an embedded control board equipped with Bluetooth and WiFi modules. These modules connect the Android app to the data acquisition board. The control board receives configuration and acquisition commands from the app, which are then parsed and forwarded to the acquisition board. The control board also processes the data collected by the acquisition board and uploads it to the Android app after packaging.

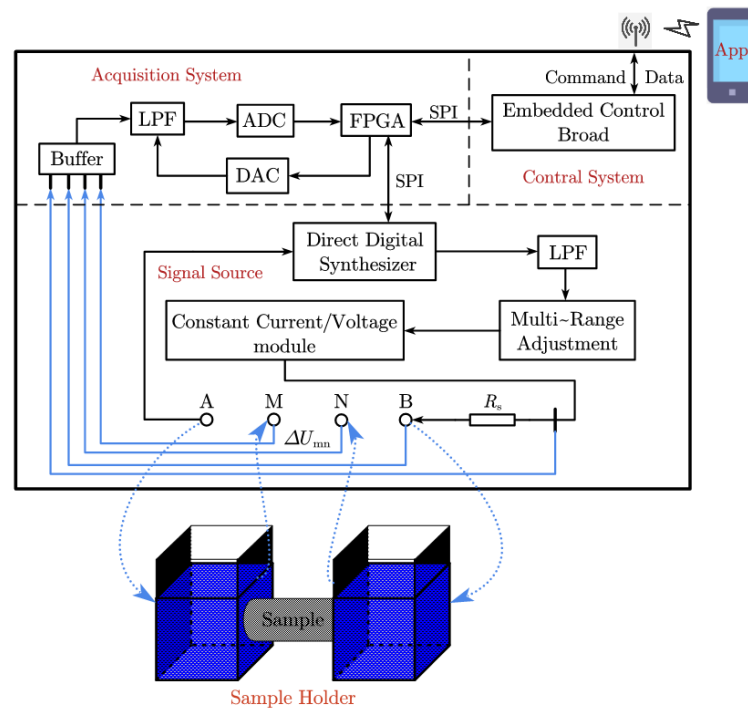


Figure 1. Structural diagram of the broadband rock and ore electrical measurement system. The signal source generates a highly stable driving signal via a direct digital synthesizer (DDS) and a constant current/voltage module, which is further adapted to diverse measurement requirements through a multi-range adjustment module. During the measurement process, the voltage difference (ΔU_{mn}) across the two ends of the sample holder is detected. The signal is subsequently filtered through a low-pass filter (LPF) before being digitized by an analog-to-digital converter (ADC) and analyzed by a field-programmable gate array (FPGA) for data processing and logical control. The system transmits data and commands to an embedded control board via a serial peripheral interface (SPI) and supports visualization and remote communication through a mobile application.

The signal source uses a board-level signal generator that provides sinusoidal signals at different frequency settings. It offers multiple adjustment levels to achieve five constant voltage outputs (1 mV, 10 mV, 100 mV, 1 V, and 10 V) and five constant current outputs (1 μ A, 10 μ A, 100 μ A, 1 mA, and 10 mA). The signal frequency accuracy reaches 0.1 ppm, ensuring distortion-free excitation of the samples.

The high-precision acquisition system is designed with four acquisition channels. The core component of the system is the FPGA model XC7K325T-2FFG900I. This system uses ultra-high input impedance (>1 G Ω) technology to reduce channel leakage currents. The voltage and current resolutions are 1 μ V and 1 nA, respectively. Additionally, the instrument is equipped with an adaptive sampling resistor network, extending the resistance range to 50 Ω –10 M Ω . During testing, the system can automatically match the sampling resistor to the actual impedance of the sample, accommodating the measurement requirements of high-impedance rock and ore samples.

The Android app, serving as the control software, is responsible for sending configuration and control commands, as well as receiving and storing data. It also includes impedance calculation and data calibration algorithms for real-time graphical data display, enabling users to easily control and monitor the system. Data communication between the app and the embedded control board is facilitated through Bluetooth and WiFi protocols, with Bluetooth handling control commands and WiFi managing real-time data transmission.

To meet the testing requirements of different samples, we designed two sets of sample holders. These sample holders are connected to the instrument using BNC triple-coaxial shielded cables, eliminating errors caused by electromagnetic coupling in the four-electrode method.

2.2. System Error Analysis

In the measurement system, the factors that most often affect the instrument’s accuracy are the distributed capacitance in the acquisition channels and the device effects caused by the sample holder. We have illustrated a simplified circuit model, as shown in Figure 2. Let $\Delta U_{mn} = U_m - U_n$ represent the voltage measured across the sample, and $\Delta U_{mn}' = U_m' - U_n'$ represent the actual voltage across the sample. I_x and I_s denote the current passing through the sample and the sampling resistor R_s , respectively. At low frequencies (<100 Hz), these effects can often be minimized through careful design of the acquisition circuit and optimization of the measurement apparatus. Under such conditions, according to Ohm’s law, the impedance of the sample is given by:

$$Z_x = |Z_x|e^{j\varphi_x} = \frac{\Delta U_{mn}'}{I_x} = \frac{\Delta U_{mn}}{I_s} = |Z_m|e^{j\varphi_m} = Z_m \tag{1}$$

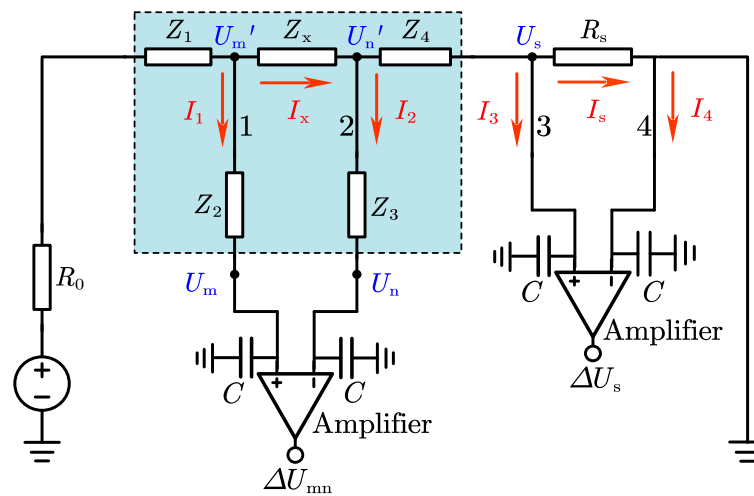


Figure 2. Simplified circuit model of the complex resistivity measurement system. After being generated by the signal source, the signal flows through the sample (Z_x) and the sampling resistor (R_s) and is subsequently processed by a differential amplifier to yield the output signal (ΔU_{mn} , U_s). However, the measurement accuracy is influenced by contact impedances (Z_1, Z_2, Z_3, Z_4) introduced by the measuring instruments, as well as leakage currents caused by the distributed capacitance (C) of the acquisition channels.

In Equation (1), Z_x represents the actual impedance of the measured sample, with $|Z_x|$ and φ_x corresponding to its impedance magnitude and phase angle, respectively. Similarly, Z_m represents the impedance value calculated by the instrument, with $|Z_m|$ and φ_m corresponding to its impedance magnitude and phase angle.

However, as the measurement frequency increases, the errors introduced by the parasitic capacitance of the internal electronic components, the contact impedance of the measuring device, and the electromagnetic coupling effects between electrodes significantly intensify, making their impact on the measurement accuracy of the instrument non-negligible. This is particularly true for soil or non-mineralized rock samples, with a weak self-polarization effect. To accurately characterize the polarization characteristics of such samples, it is necessary to analyze the error response of the measurement system.

In Figure 2, the dark box area represents the device effects of the sample holder. Z_1 and Z_4 indicate the parasitic impedance between the power supply electrodes and the receiving electrodes, while Z_2 and Z_3 denote the contact impedance between the acquisition channel and the receiving electrode. Additionally, the circuit model includes the internal acquisition circuit of the instrument, where R_0 represents the internal resistance of the signal source, and R_s denotes the sampling resistance. For the sake of analysis, we utilize a

capacitor C to simulate the distributed capacitance arising from leakage currents on the four acquisition channels, typically on the order of picoFarads (pF), with impedance defined as $Z_c = 1/(i\omega C)$, where ω is the angular frequency, and i is the imaginary unit. In the circuit model diagram, I_1 , I_2 , I_3 , and I_4 represent the magnitude of the leakage currents flowing through the four channels; therefore, the actual current flowing through the sample is given by $I_x = I_2 + I_3 + I_5$. Based on the principle of current division, we can derive:

$$I_3 = I_s \frac{R_s}{Z_c}, I_2 = \frac{(I_3 + I_5)Z_4 + I_5 R_s}{Z_c + Z_3} \quad (2)$$

By combining Equation (2), we obtain:

$$I_x = I_s \frac{(Z_3 + Z_c + Z_4)(R_s + Z_c) + R_s Z_c}{Z_c(Z_3 + Z_c)} \quad (3)$$

Similarly, based on the principle of voltage division in circuits:

$$\frac{U_m}{U_m'} = \frac{Z_c}{Z_c + Z_2}, \frac{U_n}{U_n'} = \frac{Z_c}{Z_c + Z_3} \quad (4)$$

Substituting $\Delta U_{mn} = U_m - U_n$ and $\Delta U_{mn'} = U_m' - U_n'$ into Equation (4):

$$\Delta U_{mn'} = \Delta U_{mn} + \frac{Z_2 U_m - Z_3 U_n}{Z_c} \quad (5)$$

In actual testing, Z_2 and Z_3 are often caused by the resistance of the electrodes themselves or the resistance of the electrolyte. Thus, $Z_2 \approx Z_3 = Z_{2,3}$, and therefore Equation (5) can be simplified as:

$$\Delta U_{mn'} \approx \Delta U_{mn} + \frac{Z_{2,3} \Delta U_{mn}}{Z_c} \quad (6)$$

In the current and voltage calibration equations discussed above, we primarily considered the effects of parasitic capacitance in the acquisition channels and the device effects of the measurement system itself. These considerations are based on the assumption that the electronic components selected in the circuit design are ideal. However, even high-precision resistors are subject to parasitic capacitance and lead inductance effects [36]. For instance, a 10 k Ω resistor with a 1 pF parasitic capacitance can produce a phase shift of 6 mrad at 100 kHz. These subtle parasitic capacitances similarly affect the final measurement results. To accurately measure the spectral response characteristics of high-impedance samples, this instrument uses sampling resistors up to 10 M Ω . Therefore, it is necessary to account for the parasitic capacitance of the sampling resistors in the calibration model.

3. Analysis and Calibration of the Instrument's Acquisition Circuit

The distributed capacitance of the instrument's internal acquisition channels can significantly affect data collection. This distributed capacitance creates a low-pass filtering effect that attenuates high-frequency signals, leading to waveform distortion and phase shifts. This manifests in the circuit as leakage currents, which reduce the input impedance of the instrument and consequently decrease measurement accuracy [37]. This impact is predominantly observed at high frequencies, as the internal distributed capacitance of the instrument is typically in the picoFarad (pF) range, exerting minimal influence at low frequencies.

Figure 3 displays the instrument response results (uncalibrated) of the CSUZA-FW08 when testing a 100 Ω pure resistor, employing an adaptive testing method. In this scenario, the instrument selects a sampling resistor (100 Ω) that closely matches the sample's resistance for measurement. When the frequency is below 1 kHz, the instrument's resistance

measurement accuracy can reach 0.3%, while the phase measurement accuracy can achieve 0.1 mrad. However, at high frequencies (>1 kHz), both the resistance and phase begin to deviate from their actual values, with phase shifts reaching up to 2.8 mrad at 100 kHz. This testing result primarily reflects the influence of the distributed capacitance within the instrument’s internal acquisition channels. This effect further intensifies as the resistance of the measured sample increases, potentially obscuring the intrinsic polarization characteristics of the rock samples. To minimize the impact on test results, it is essential to analyze the magnitude of the channel’s distributed capacitance, compensate for measurement errors, and address circuit design and component selection. We designed two circuit models for analysis, placing the sampling resistor at the end of the circuit or on the signal source side. This can be easily achieved by altering the connection direction of the signal source, thus referring to these configurations as the direct connection and reverse connection forms of the signal source. We will compare the advantages, disadvantages, and differences between these two circuit design forms.

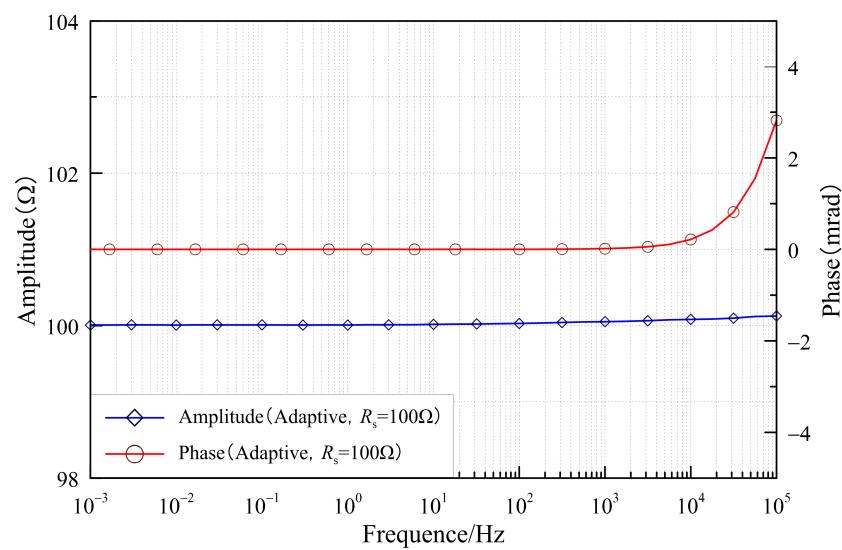


Figure 3. Impedance measurement results of a 100 Ω resistor under the influence of distributed capacitance in the acquisition channel.

3.1. Forward Connection of the Signal Source

In the first circuit design model (Figure 4), the sampling resistor R_s is positioned at the end of the circuit, which is a commonly adopted design scheme in impedance analyzers [27,29].

To analyze the measurement errors within the instrument independently, we employed a BNC tri-coaxial shielded cable for direct resistance measurement. In this configuration, the error terms related to the measurement device, $Z_1, Z_2, Z_3,$ and $Z_4,$ can be neglected, leading to a simplified circuit diagram as shown in Figure 4. The measurement errors are primarily induced by the leakage currents I_2 and I_3 of the second and third acquisition channels, while the fourth acquisition channel is short-circuited. In this circuit model, the actual current I_x flowing through the sample can be simplified from Equation (3) as follows:

$$I_x = I_s + I_2 + I_3 = I_s(1 + 2R_s\omega Ci) \tag{7}$$

Similarly, the actual voltage value across the sample, $\Delta U_{mn} = \Delta U_{mn}'$. The actual impedance of the measured resistor can be calculated as:

$$Z_x = \frac{\Delta U_{mn}'}{I_x} = \frac{\Delta U_{mn}}{I_s(1+2R_s\omega Ci)} = \frac{Z_m}{1+2R_s\omega Ci} \tag{8}$$

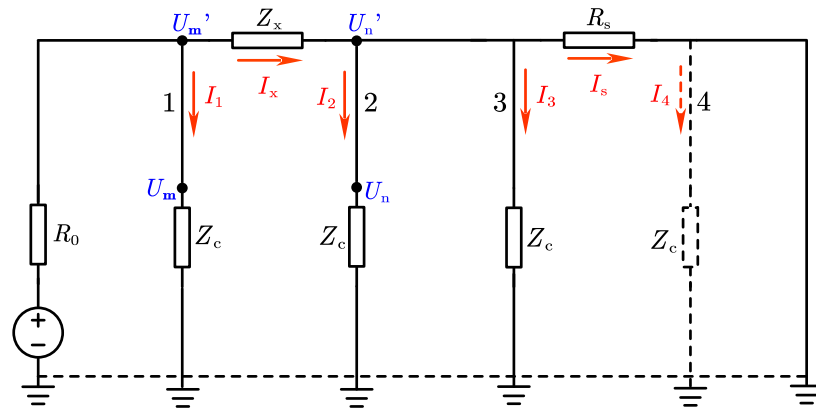


Figure 4. Simplified acquisition circuit diagram with forward connection of signal source, with sampling resistor positioned at the terminal far from the signal source. After being generated by the signal source, the signal flows through the sample Z_x and then to the sampling resistor R_s . Due to the presence of distributed capacitance in the acquisition channels, a leakage current I_1, I_2, I_3, I_4 is introduced, resulting in a discrepancy between the currents I_x and I_s .

In Equation (8):

$$1 + 2R_s\omega Ci = \sqrt{1 + (2R_s\omega C)^2} e^{\tan^{-1}(2R_s\omega C)} \quad (9)$$

The operating frequency range of the complex resistivity measurement system is from 1 mHz to 100 kHz, with an angular frequency $\omega = 2\pi f < 6.3 \times 10^5$ rad/s. Due to the distributed capacitance C being in the picoFarad (pF) range, when the sampling resistor R_s has a relatively low resistance (< 1 k Ω), $2R_s\omega C < 0.1$. Thus, Equation (9) can be simplified as follows:

$$1 + 2R_s\omega Ci \approx e^{2R_s\omega Ci} \quad (10)$$

The error between the actual impedance of the sample and the measured impedance is given by:

$$Z_x = \frac{Z_m}{1 + 2R_s\omega Ci} \approx \frac{|Z_m|e^{i\phi_m}}{e^{2R_s\omega Ci}} = |Z_m|e^{i(\phi_m - 2R_s\omega C)} \quad (11)$$

From the above equation, it is evident that the impedance measurement error is primarily reflected in the phase and is solely related to the value of the sampling resistor R_s , independent of the intrinsic impedance characteristics of the measured sample. When the sampling resistor R_s is small, the calibration method is simple and quick, making it a commonly adopted calibration scheme. However, as the value of the sampling resistor R_s increases, the impedance measurement error will rapidly escalate, complicating the calibration process, and the influence of the parasitic capacitance of the sampling resistor will also intensify. Therefore, this circuit model limits the range of sampling resistor values, rendering it inadequate for the measurement needs of high-impedance samples.

3.2. Reverse Connection of the Signal Source

We compared the impedance measurement errors of the second circuit configuration, as shown in Figure 5. In this case, the sampling resistor is positioned on the output source side, which can be achieved by interchanging the connections of the signal source, referred to as the reverse connection of the signal source.

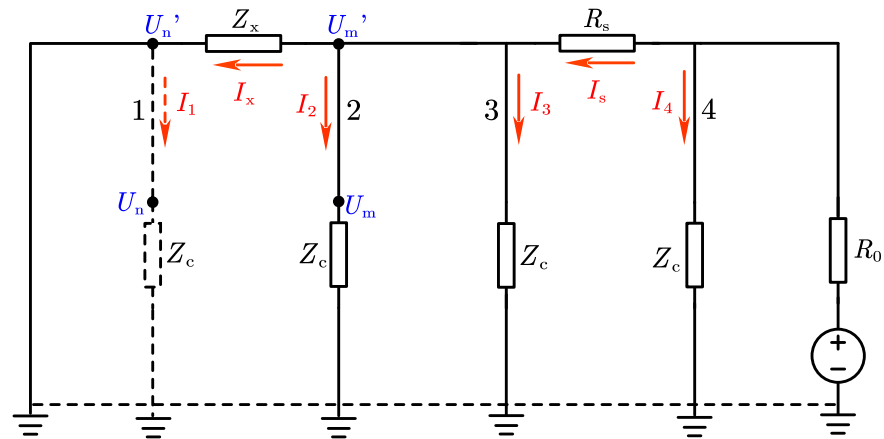


Figure 5. Simplified acquisition circuit diagram with reverse connection of signal source, with sampling resistor positioned at the front end near the signal source. After being generated by the signal source, the signal flows through the sampling resistor R_s and then to the sample Z_x . Due to the presence of distributed capacitance in the acquisition channels, a leakage current I_1, I_2, I_3, I_4 is introduced, leading to a discrepancy between the currents I_x and I_s .

In this circuit model, the current I_x is expressed as $I_x = I_s - I_2 - I_3$, and the voltage difference ΔU_{mn} is equivalent to $\Delta U_{mn}'$. The measurement error in impedance is predominantly influenced by leakage currents associated with both the two-channel and three-channel configurations:

$$Z_x = \frac{\Delta U_{mn}'}{I_x} = \frac{\Delta U_{mn}}{I_s - \frac{2U_m}{Z_c}} = \frac{Z_m}{1 - 2Z_m\omega C i} \quad (12)$$

Similarly, when the resistance of the measured sample is relatively low, given that $2|Z_m|\omega C < 0.1$, the impedance $Z = |Z|\cos\varphi + |Z|\sin\varphi i$ can be approximated as $Z \approx |Z| + |Z|\varphi i$ when the absolute value of the phase angle $|\varphi|$ is small. Thus:

$$Z_x = \frac{Z_m}{1 - 2Z_m\omega C i} \approx \frac{|Z_m|e^{i\varphi_m}}{e^{-2|Z_m|\omega C i}} = |Z_m|e^{(\varphi_m + 2|Z_m|\omega C)i} \quad (13)$$

$$\Delta U_{mn}' \approx \Delta U_{mn} + \frac{Z_{2,3}\Delta U_{mn}}{Z_c} \quad (14)$$

At this stage, the measurement error primarily manifests in the phase, and its magnitude exhibits a similar pattern to the forward connection, albeit with an opposite sign. However, the phase error is independent of the sampling resistance and is solely related to sample impedance. When the impedance Z_x is low, we can utilize this approach to calculate the parasitic capacitance C of the internal channels of the instrument, which has been measured to be approximately 24 pF. However, as Z_x increases, Z_m also increases, leading to a larger measurement error with a more complex error pattern.

3.3. Correction Methods Based on Forward and Reverse Connection Circuit Configurations of the Signal Source

Based on the above two circuit configurations, the first method, although primarily dependent on the sampling resistance and therefore more convenient for calibration, poses challenges for high-impedance samples. For certain dense surrounding rocks, the sample resistance can exceed 10 MΩ, whereas the polarization effects remain minimal. In this scenario, employing a small sampling resistance for measurements will lead to increased errors in resistance calculations. Conversely, utilizing a large sampling resistance will cause the phase shift due to the components' parasitic capacitance at high frequencies, which will sig-

nificantly affect the phase measurement results of low-polarization samples. To accurately characterize the internal measurement errors of the instrument, it is essential to consider the parasitic capacitance of the sampling resistance concurrently. Consequently, the current I_x flowing through the sample in the first circuit configuration (forward connection) should be modified according to Equation (7):

$$I_x = I_s' + I_2 + I_3 = I_s' + 2I_s R_s \omega C i = I_s \left(\frac{I_s'}{I_s} + 2R_s \omega C i \right) = I_s \left(\frac{R_s}{Z_s} + 2R_s \omega C i \right) \quad (15)$$

I_s' represents the actual current flowing through the sampling resistance Z_s in Equation (15). Substituting the equation back into Equation (8) yields:

$$Z_x = \frac{\Delta U_{mn}}{I_s \left(\frac{R_s}{Z_s} + 2R_s \omega C i \right)} = \frac{Z_m}{R_s} \frac{Z_s}{1 + 2Z_s \omega C i} \quad (16)$$

In the reverse connection configuration of the signal source, the current I_x flowing through the actual sample is expressed as:

$$I_x = I_s' - I_2 - I_3 = I_s' - 2I_s Z_m \omega C i = I_s \left(\frac{I_s'}{I_s} - 2Z_m \omega C i \right) = I_s \left(\frac{R_s}{Z_s} - 2Z_m \omega C i \right) \quad (17)$$

Equation (12) is transformed to:

$$Z_x = \frac{\Delta U_{mn}}{I_s \left(\frac{R_s}{Z_s} - 2Z_m \omega C i \right)} = \frac{Z_m}{\frac{R_s}{Z_s} - 2Z_s \omega C i} \quad (18)$$

To characterize the error between the actual impedance Z_s of the sampling resistance and the calculated value R_s , we connect a component identical to the sampling resistance in the BNC measurement line as the test resistance, i.e., $Z_x = Z_s$. Equation (18) can be transformed to:

$$Z_m = \frac{R_s}{1 + 2Z_s \omega C i'} \quad (19)$$

To differentiate the measured values Z_m in Equations (16) and (19), we denote the measurement in Equation (16) as Z_{m1} and that in Equation (19) as Z_{m2} , representing the measurements obtained under the forward and reverse connection configurations of the signal source, respectively. By combining these two equations, we obtain:

$$Z_x = \frac{Z_{m1} Z_{m2} Z_s}{R_s^2} = \frac{|Z_{m1}| |Z_{m2}| |Z_s|}{R_s^2} e^{(\varphi_{m1} + \varphi_{m2} + \varphi_s) i} \quad (20)$$

In Equation (20), $|Z_{m1}|$, $|Z_{m2}|$, $|Z_s|$ and φ_{m1} , φ_{m2} , φ_s represent the magnitudes and phases of the impedances Z_{m1} , Z_{m2} , and Z_s , respectively. From Equation (20), it is evident that the actual impedance of the sample is related to the measured values Z_{m1} and Z_{m2} under the forward and reverse connection configurations of the signal source, as well as the actual impedance Z_s and calculated value R_s of the sampling resistance. The phase error is primarily influenced by φ_{m1} , φ_{m2} , and φ_s , where φ_{m1} and φ_{m2} are mainly determined by the parasitic capacitance distribution within the instrument. In contrast, φ_s is affected by the parasitic capacitance of the components themselves. When the sampling resistance is low and the measured impedance $Z_x = Z_s$, we have $|Z_{m1}| \approx |Z_{m2}| \approx |Z_s| \approx R_s$ and $\varphi_s \approx 0$, leading to $\varphi_{m1} = -\varphi_{m2}$. This conclusion is consistent with Equations (11) and (14). Essentially, Equation (20) generalizes the error term by considering the parasitic capacitance of the sampling resistance, thus enhancing calibration accuracy. Additionally, the form of this error term is simple and facilitates calibration

without the need for separate analysis of the internal channel distribution capacitance C . The sampling resistance R_s does not need to be limited to low values. By calculating the actual impedances Z_s of different sampling resistances and the measured values Z_{m2} for the reverse connection configuration using standard components, this information can be integrated into the data acquisition program to enable automatic data calibration for varying sample impedances under the forward connection configuration. It is important to note that the forward and reverse connection testing method does not require two measurements for each sample, as this would significantly reduce acquisition efficiency. During normal testing, the forward connection configuration of the signal source is still employed, while the reverse connection configuration functions similarly to the calibration process. Calibration data for different sampling resistances can be established once, and the capability to switch between forward and reverse connections can be integrated into the App control interface for user convenience.

To further validate the accuracy of the analytical results, a low-resistance testing model with a pure resistance of $1\text{ k}\Omega$ was designed. Adaptive testing of the sampling resistance (also set at $1\text{ k}\Omega$) was conducted under both the signal source's forward and reverse connection configurations. The test results before calibration are shown in Figure 6. The phase curves for the forward and reverse connections satisfy $\varphi_{m1} = -\varphi_{m2}$, and the resistance magnitudes $Z_{m1} \times Z_{m2} = R_s^2$, consistent with the characteristics outlined in Equation (20).

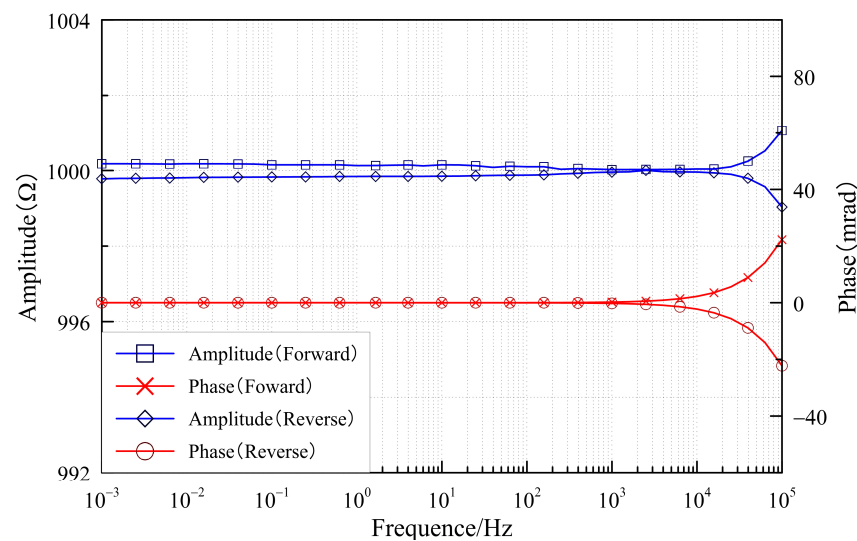


Figure 6. Impedance test results for a $1\text{ k}\Omega$ resistor using forward and reverse connection methods of the signal source, showing uncalibrated data.

Conventional data calibration methods generally utilize the forward connection of the signal source, with calibration performed using Equation (11). To reduce the influence of the sampling resistor on calibration accuracy, sampling resistors with values below $1\text{ k}\Omega$ are commonly selected. In this study, a forward-reverse switching approach for the signal source connection is adopted. Initially, the reverse connection is employed to calibrate sampling resistors with a wide range of resistances ($50\ \Omega$ – $10\text{ M}\Omega$). The forward connection is then used to obtain the raw complex resistivity data of rock samples prior to calibration. Finally, the data is calibrated using Equation (20). This method offers the advantage of eliminating the restriction to low-value sampling resistors (below $1\text{ k}\Omega$) by calibrating the parasitic capacitance of large sampling resistors, thereby enabling high-precision measurements for high-impedance samples. To evaluate the method, a $10\text{ k}\Omega$ pure resistor model was tested and calibrated using both the traditional forward connection method and the proposed forward-reverse switching

method, as shown in Figure 7. The results indicate that the proposed method achieves superior resistance accuracy. While phase deviations were observed at high frequencies, measurements conducted using an LCR bridge instrument revealed that the parasitic capacitance of the 10 kΩ resistor is approximately 0.46 pF, with the theoretical phase at 100 kHz being about 2.9 mrad, closely matching the calibration results.

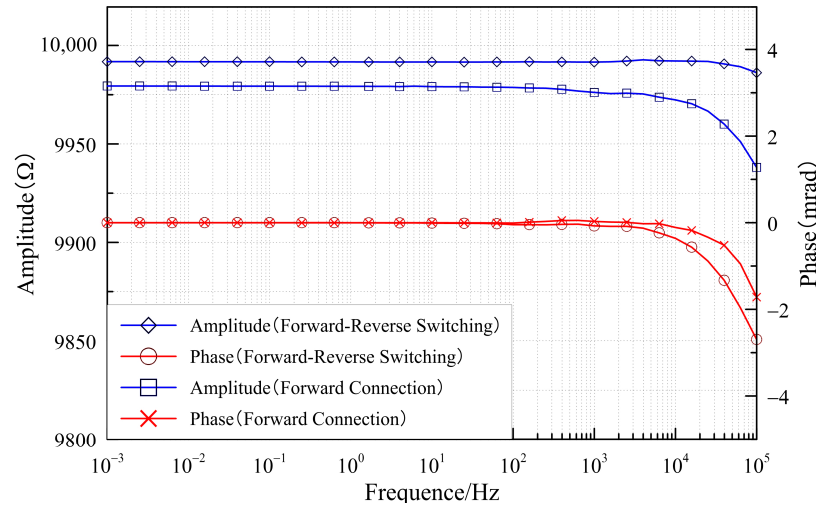


Figure 7. Comparison of impedance test results for a 10 kΩ resistor using adaptive and non-adaptive sampling resistance methods, with the non-adaptive method employing a 1 kΩ sampling resistor.

Figure 8 presents the test results for three sets of parallel resistor-capacitor models. The product of resistance R and capacitance C for each model is kept consistent, with varying values employed to assess whether the instrument can achieve the same accuracy under different sampling resistances. The resistance and capacitance values for the three sets of models are detailed in Table 1. The testing results show that the precision of the first two sets is within 1%, showing good agreement with the theoretical curves. However, the phase curve of the third set exhibits slight deviations from the theoretical values. Measurements taken with an LCR bridge indicate that the parasitic capacitance of the 100 kΩ component is approximately 0.6 pF, while in the third model, the capacitance $C_3 = 8$ pF, resulting in lower phase measurement results during actual testing.

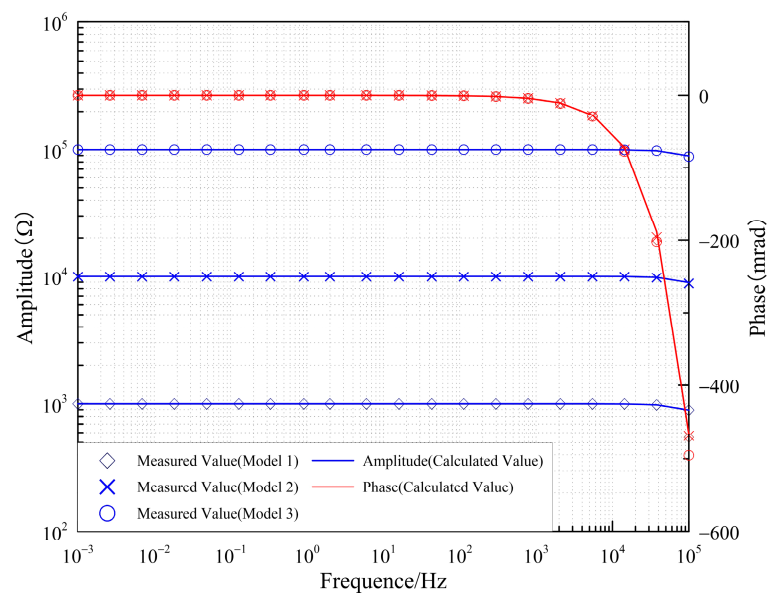
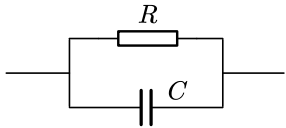


Figure 8. Impedance comparison test results for the three resistor-capacitor models.

Table 1. Resistance and capacitance values for the three resistor-capacitor models.

Model	R/Ω	C/pF
1	1 k	800
2	10 k	80
3	100 k	8



4. Design and Calibration of the Measurement Instrument

In addition to the internal calibration of the instrument, the influence of the measurement device on the test results is also highly significant. The distinction between the rock and ore electrical measurement instruments and traditional impedance analyzers lies in the specific measurement objects. Enhancing the measurement accuracy of the rock sample’s resistivity and providing a reasonable and practical sample holder design are the primary tasks in developing this instrument.

In Figure 2, the dark box portion represents the device effects of the sample holder, where Z_1 and Z_4 denote the stray impedances between the measuring and receiving electrodes. In contrast, Z_2 and Z_3 represent the contact impedances between the acquisition channels and the measuring electrodes. These error terms may vary depending on the specific measurement device used. Referring to Figure 2, the actual current I_x flowing through the sample is given by:

$$I_x = I_s' + I_2 + I_3 = I_s R_s \left(\frac{1}{Z_s} + \frac{2}{Z_c} + \frac{Z_4}{Z_c^2} + \frac{Z_4}{Z_c Z_s} \right) \tag{21}$$

By substituting Equation (5) into Equation (21), we obtain the actual impedance value Z_x of the sample, taking into account the device effects:

$$Z_x = \frac{Z_m}{R_s} \frac{Z_s(1 + Z_{2,3}\omega Ci)}{1 + 2Z_s\omega Ci + Z_4\omega Ci - Z_4Z_s\omega^2 C^2} \tag{22}$$

To analyze the impact of the measurement device on the test results, we designed the circuit model shown in Figure 9a. With $Z_x = 1\text{ k}\Omega$ and $Z_2 = Z_3 = 100\ \Omega$ held constant, we varied the values of Z_1 and Z_4 . Figure 9b displays the phase test results of the instrument before calibration for different values of Z_1 and Z_4 , compared with the calculated results from Equation (22). The results indicate that the calculated curve aligns with the measured results, and as the contact impedances Z_1 and Z_4 increase, the measurement errors gradually expand.

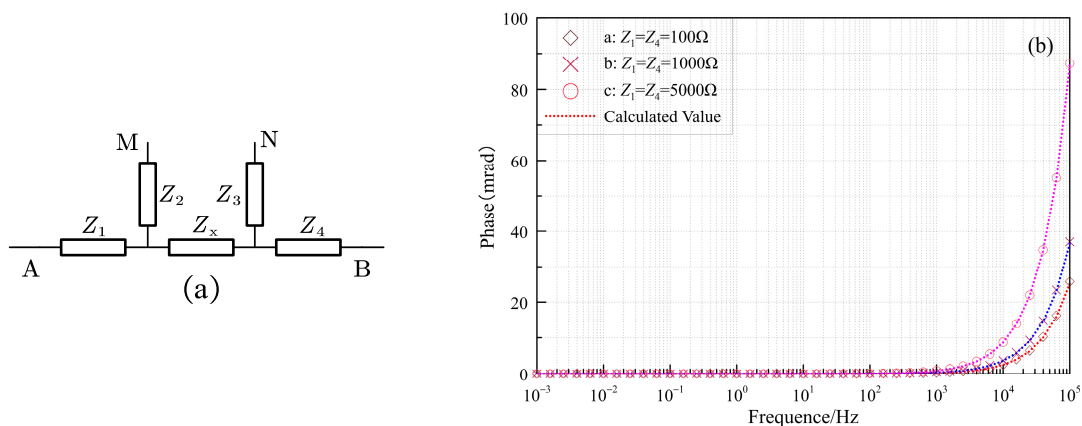


Figure 9. (a) Diagram of the designed circuit model, and (b) Comparison of the phase testing results of this model (before calibration) with the calculated results obtained from Equation (22) upon varying the values of Z_1 and Z_4 .

In this study, we designed two measurement devices for different testing subjects. We chose the sample holder shown in Figure 10a for the measurement of rock and ore samples. We selected the device depicted in Figure 10b to test loose materials such as rock fragments and soil or for liquids. In both measurement setups, Z_2 and Z_3 represent the actual impedance of the electrodes, which is less than 1Ω , thus $Z_2 \approx Z_3 = Z_{2,3} \ll Z_{in}$ (where Z_{in} denotes the input impedance of the instrument's acquisition channel, which is approximately $17 \text{ G}\Omega$ for this device). Additionally, $Z_4 Z_s \omega^2 C^2 \ll 1$. Combining this with the results from the different sampling resistance reverse connection methods in Equation (19), we can transform Equation (22) to:

$$Z_x = \frac{Z_{m1} Z_{m2} Z_s}{R_s^2 + Z_4 Z_{m2} \omega C i} \quad (23)$$

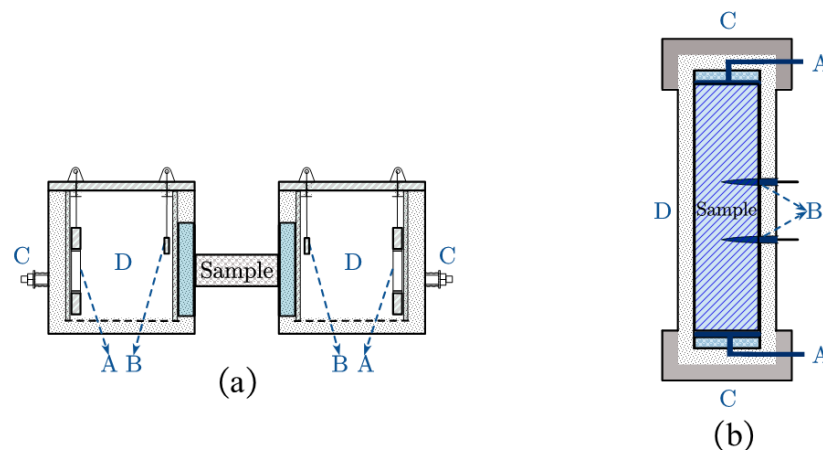


Figure 10. Schematic diagrams of two measurement devices: (a) the diagram used for measuring standard rock samples such as ores, and (b) the device employed for testing solutions and loose samples.

The sample holder shown in Figure 10a can be divided into four parts: A for the power electrodes; B for the measurement electrodes; C for the fixture, and D for the sample holder container. During the design process of the sample holder using the four-electrode method, the electromagnetic coupling between the measurement electrodes and measurement lines is the primary concern, particularly affecting measurements at frequencies above 1 kHz and increasing with frequency. Therefore, BNC triple coaxial shielded cables were selected to connect the measurement device to the equipment. The sample holder is made of polymer materials, providing excellent electrical insulation and chemical corrosion resistance. Furthermore, the current electrodes (power electrodes) and voltage electrodes (measurement electrodes) are made from copper alloy, with an area of $10 \text{ cm} \times 10 \text{ cm}$. This ensures good oxidation resistance to effectively mitigate the impact of low-frequency electrode polarization on data results. This also facilitates uniform current flow through the sample. A saturated CuSO_4 solution is placed within the sample holder container to minimize electrochemical reactions with the electrodes. Additionally, the CuSO_4 electrolyte technology solution reduces the electrolyte's resistivity to a minimum (with resistivity less than $0.1 \Omega \cdot \text{m}$), allowing Z_1 and Z_4 to drop below 1Ω , making their impact on the measurement results negligible. Data calibration can be performed using Equation (20). The sample holder is designed for convenience and ease of operation and is secured by a support frame to ensure sample stability during testing. A copper sulfate paste contacts the voltage electrode and the sample, reducing contact impedance. To prevent creeping currents on the rock's surface and evaporation of moisture during testing, plastic wrap can cover the sides of the rocks.

The device shown in Figure 10b meets the corresponding requirements for testing sand and liquids. This design can also be divided into four parts: A for the power electrodes; B for the measurement electrodes; C for the base; and D for the sample container. Acrylic glass is chosen as the design material for this sample holder. To minimize the impact of power electrode polarization on the measurement electrode, the distance between the two should be approximately twice the sample spacing (i.e., the spacing between the measurement electrodes) [27]. The power electrodes remain made of copper alloy, but the measurement electrodes are altered. For rock samples testing, planar electrodes are selected to maximize the contact area with the sample, thereby reducing transition resistance. In contrast, point-type AgCl electrodes are used for water or sand tests to minimize errors caused by poor coupling between the electrode and sample [4]. The AgCl electrodes exhibit strong electrochemical stability and minimal polarization effects. In this case, the stray impedances Z_1 and Z_4 between the power electrode and measurement electrode are primarily induced by the sample itself and cannot be neglected; therefore, calibration should be performed using Equation (23).

To verify the calibration effectiveness of the measurement device, we designed a circuit model to simulate the polarization characteristics of samples and the device effects during actual rock sample testing, as shown in Figure 11. The figure presents a comparison between the calibrated test results and the theoretical results. It demonstrates a phase shift occurring between 1 Hz and 10 kHz, simulating the low-frequency double-layer polarization effects in rock and ore samples. After 10 kHz, the phase exhibits a downward trend again, simulating the high-frequency interface polarization effects. The calibrated test results show a high degree of consistency with the theoretical values, validating the accuracy of the calibration algorithm.

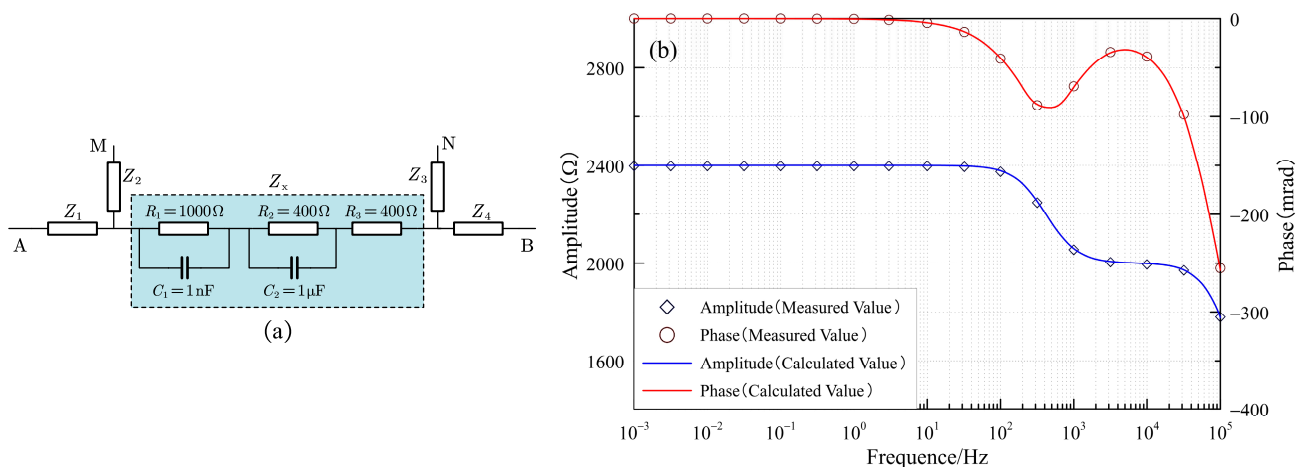


Figure 11. (a) Diagram of the designed circuit model, and (b) Comparison of the impedance testing results of the model after calibration using Equation (23) with the calculated results.

Subsequently, we analyzed the testing performance of the sample holder shown in Figure 10a. Figure 12 compares the spectral curves of a limestone sample before and after calibration. This sample exhibits low resistance and polarization characteristics due to its well-developed porosity, resulting in a lower resistivity. It does not contain metallic mineral conductors that would cause significant polarization effects, with interface polarization effects only observed at high frequencies. After calibration, the actual proper response characteristics of the sample were effectively restored, with phase errors primarily evident in the high-frequency region (>1 kHz), reaching 42 mrad at 10^5 Hz. Therefore, calibration of high-frequency test data is necessary.

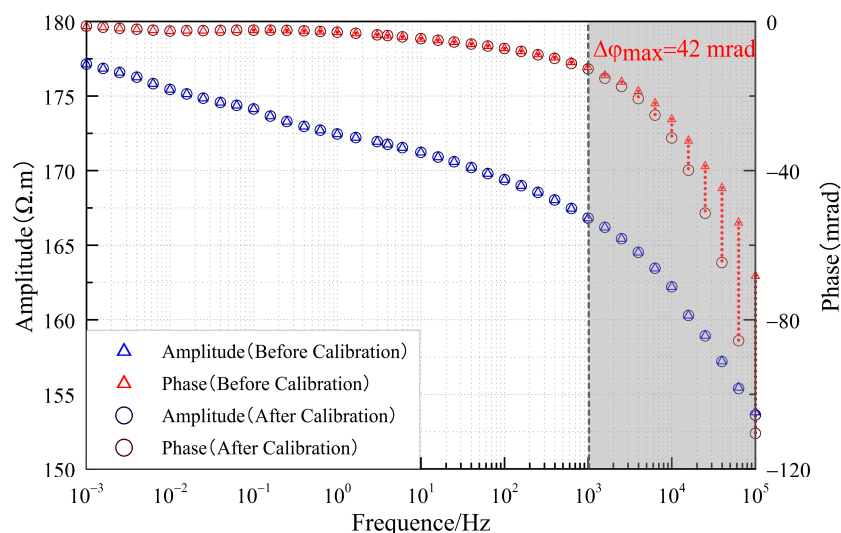


Figure 12. Complex resistivity testing results of the limestone sample before and after calibration.

5. Results

In this section, multiple circuit models were designed for testing, comparing the measurement accuracy of our instrument with the Solartron 1260A impedance analyzer. Combined with the test results from rock and ore samples as well as NaCl solutions, we analyzed the overall stability and accuracy of the measurement system, further validating the effectiveness of the calibration algorithm. First, we tested the impedance values of pure resistances of 1 k Ω and 1 M Ω (Figure 13), comparing them with the results from the Solartron 1260A impedance analyzer. For the low resistance test, the results from both instruments were similar, with a high-frequency phase shift of approximately 0.5 mrad, and both the resistance and phase curves were relatively smooth, indicating good instrument stability. However, the results from the two instruments showed significant discrepancies in the tests involving more extensive, more significant sampling resistances. Our instrument exhibited a more petite polarization shift at high frequencies than the Solartron 1260A. The internal parasitic capacitance of the tested 1 M Ω resistor was determined to be approximately 0.50 pF, with a theoretical phase shift of around 300 mrad, which aligns closely with our instrument's measurements. Table 2 presents the test results for two instruments across a resistance range of 100 Ω to 10 M Ω , using test resistors with a precision of 0.5% and parasitic capacitance below 1 pF. The complex resistivity data was converted into resistance and capacitance parameters for comparison. The results reveal that as the test resistance increases, the measurement accuracy of the proposed instrument (CSUZA-FW08) progressively surpasses that of the Solartron 1260A impedance analyzer. The resistance error of the CSUZA-FW08 consistently remains within 1%, while the capacitance measurements stay below 1 pF, accurately reflecting the actual characteristics of the test resistors. More significant errors observed at high frequencies with the Solartron 1260A impedance analyzer can be attributed to its input impedance (300 M Ω), much lower than that of our instrument (17 G Ω). Additionally, the small sampling resistance used resulted in decreased measurement accuracy when testing high-impedance samples. Our instrument achieves precise measurements of high-impedance samples by increasing the sampling resistance and employing an adaptive matching calibration algorithm. It is also evident that the internal parasitic capacitance of the 1 M Ω pure resistor can cause a phase shift of around 300 mrad at high frequencies. Therefore, considering the influence of the sampling resistance's parasitic capacitance in the calibration model can further enhance the accuracy of the calibration algorithm.

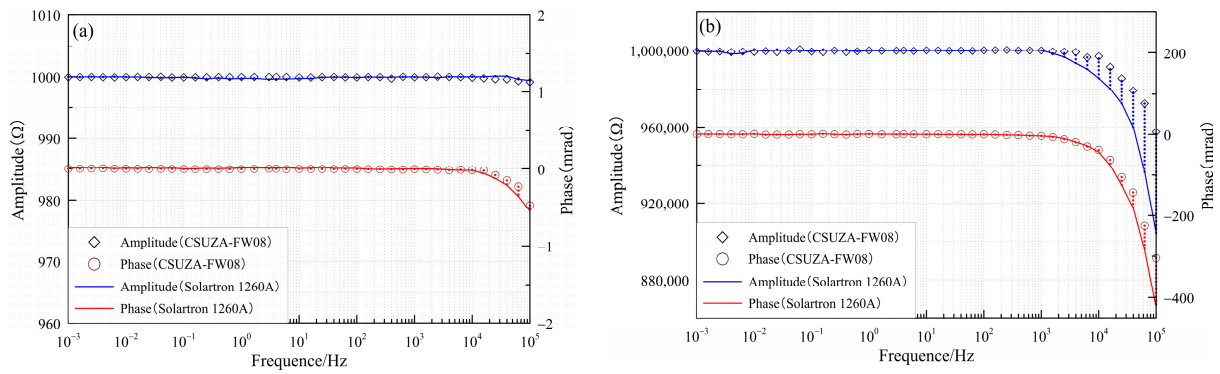


Figure 13. Comparison of the test results between the CSUZA-FW08 instrument and the Solartron 1260A impedance analyzer when measuring the resistance of 1 kΩ (a) and 1 MΩ (b).

Table 2. Comparison of measurement results between the CSUZA-FW08 instrument and the Solartron 1260A impedance analyzer when measuring different resistances.

Model	R/Ω	Measured Resistance/Ω				Measured Capacitance/pF	
		CSUZA-FW08	Error (%)	Solartron 1260A	Error (%)	CSUZA-FW08	Solartron 1260A
1	100	99.8	0.20	99.8	0.20	0.03	0.01
2	1k	1000.7	0.07	1000.4	0.04	0.42	0.44
3	10k	10,018.5	0.19	9998.7	0.01	0.44	0.47
4	100k	100,372.1	0.37	99,803.9	0.20	0.57	0.64
5	1M	1,005,816.4	0.58	989,711.0	1.03	0.48	0.70
6	10M	10,096,038.6	0.96	9,570,166.5	4.30	0.83	5.26

Figure 14 compares the complex resistivity test results between our instrument and the Solartron 1260A impedance analyzer, both using the sample holder shown in Figure 10a for measurement. The tested sample was lead-zinc ore. The results from the complex resistivity tests indicate that this sample exhibits low resistance and high polarization characteristics, with the resistivity magnitude decreasing with increasing frequency. The phase curve characterizes the sample’s double-layer polarization at low frequencies and interface polarization effects at high frequencies. The results from both instruments are similar, with smooth testing curves, indicating high stability and accuracy of the measurement system, along with strong anti-interference capability.

We also tested solution samples using the instrument shown in Figure 10b. Figure 15 compares the phase test results for NaCl solutions of different resistivities with their theoretical calculations. The spectral response characteristics of the NaCl solution at 21 °C can be calculated using Equation (24) [38]:

$$\varphi = -\arctan(\omega\varepsilon_0\varepsilon_r\rho') \tag{24}$$

In Equation (24), $\varepsilon_0 = 8.854 \times 10^{-12}$ F/m represents the vacuum permittivity, $\varepsilon_r = 79.7$ is the relative permittivity of water at 21 °C, and ρ' is the real part of the resistivity.

The results indicate a pronounced downward trend in the high-frequency phase of the NaCl solution, with the decline accelerating as the resistivity increases. Below 10 kHz, the test results remain generally consistent with the theoretical curve, with an error controlled within 0.1 mrad. Above 10 kHz, the discrepancy between the two increases yet remains within 2 mrad. The decline in high-frequency calibration accuracy may be attributed to the following two factors:

- (a) In Equation (23), the measurement results of the stray impedance Z_1 and Z_4 between the power supply electrode and the receiving electrode can influence the final calibration outcome. If we assume that the test solution is uniformly distributed within the measurement container, the relationship between the stray impedances Z_1 , Z_4 , and the impedance of the sample Z_x can be roughly estimated based on the distance AM between the measuring electrode and the receiving electrode. However, for accurate results, precise measurements of Z_1 and Z_4 should be conducted using other testing methods.
- (b) During the calibration of complex resistivity data, we primarily analyze the distributed capacitance of the instrument's acquisition channels, the parasitic capacitance of the sampling resistor, and the device effects of the sample holder. In four-point measurements, electromagnetic coupling interference must also be considered, as this effect increases with the measurement frequency.

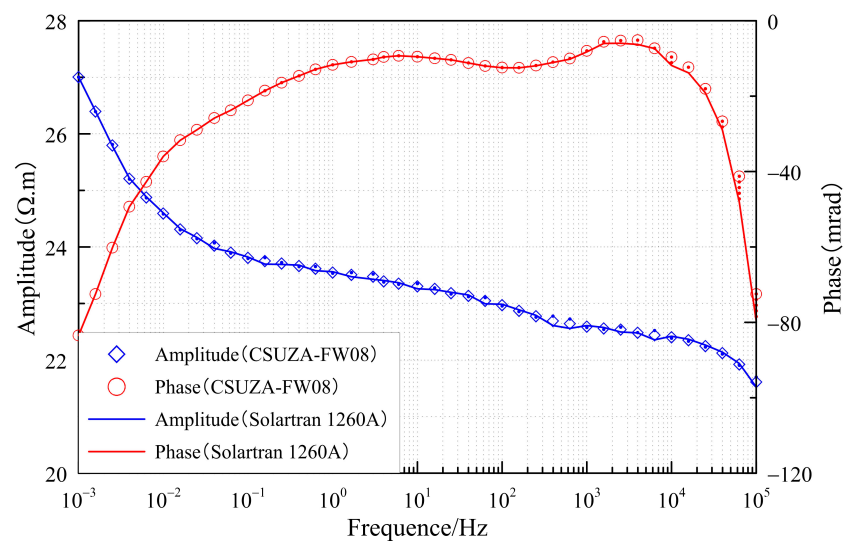


Figure 14. Comparison of the complex resistivity testing results between the CSUZA-FW08 instrument and the Solartron 1260A impedance analyzer when the sample is lead-zinc ore.

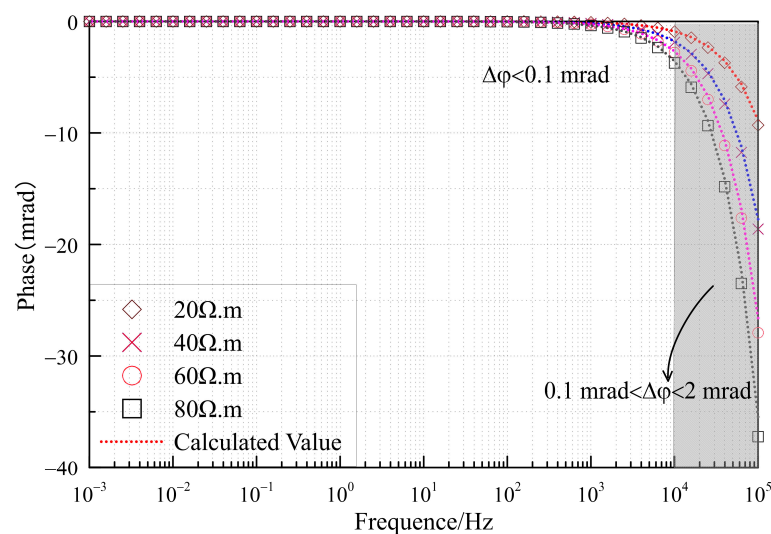


Figure 15. Comparison of the phase testing results of NaCl solutions with different resistivities against the calculated values.

Below 100 kHz, the calibration method proposed in this study can meet the demands of high-precision testing. Since testing of rock and ore samples typically does not exceed 100 kHz, this calibration method remains highly applicable.

Finally, we conducted tests on two rock samples using the proposed instrument (CSUZA-FW08) and calibration method, as shown in Figure 16. The two rock samples were collected from the Chanlinshan multimetallic mining area in Nanjing, Jiangsu Province, China, representing chalcopyrite and diorite samples. After completing the tests, we performed an inversion of the complex resistivity data of the two samples using the Cole-Cole model. The model equation is as follows:

$$\rho(i\omega) = \rho_0 \left\{ 1 - m \left[1 - \frac{1}{1 + (i\omega\tau)^c} \right] \right\} \tag{25}$$

In Equation (25):

ω represents the angular frequency, measured in rad/s.

ρ is the complex resistivity, expressed in $\Omega \cdot m$.

ρ_0 denotes the zero-frequency resistivity, which characterizes the electrical conductivity of the rock, measured in $\Omega \cdot m$.

m is the chargeability, describing the intensity of the induced polarization effect in rocks and ores.

τ is the time constant, representing the speed of the induced polarization process in rocks and ores, measured in seconds (s).

c is the frequency dependence coefficient, ranging from [0,1], which reflects the gradual or abrupt nature of the dispersion process as indicated by the shape of the dispersion curve.

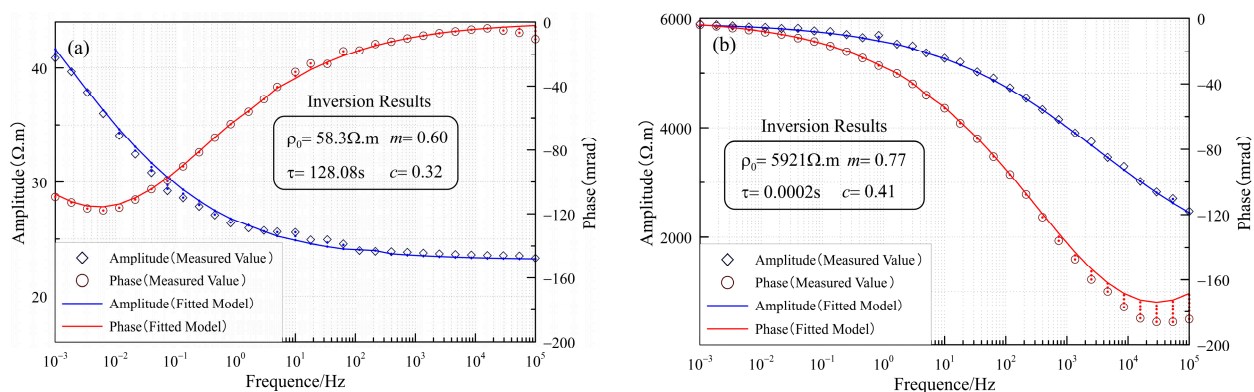


Figure 16. Inversion results of two rock samples: (a) chalcopyrite sample; and (b) diorite sample.

By comparing the test results of the two rock samples, it is evident that the chalcopyrite sample exhibits lower resistivity, and its phase curve shows a significant deviation at low frequencies, indicating a stronger polarization effect. In contrast, the diorite sample displays high-resistance characteristics, and its phase curve approaches zero at low frequencies, revealing a clear physical property difference between the two samples.

Based on the inversion results of both rock samples, the time constant of the chalcopyrite sample is significantly larger than that of the diorite sample. This parameter is often used to describe the mineralization characteristics of rock samples. Therefore, this calibration method proves to be effective in distinguishing and identifying mineralized rock samples.

6. Conclusions

This study is based on the self-developed broadband rock and ore electrical measurement system, analyzing the errors generated within the instrument due to the distributed capacitance of the acquisition channel and the parasitic capacitance of the sampling resistor. By integrating two circuit design models (signal source direct connection and reverse connection), a new calibration method for the instrument is proposed. This method requires first measuring the spectral response characteristics of different sampling resistors with the signal source reversed and incorporating these as calibration values within the testing algorithm. Subsequently, the signal source direct connection method can be used to test samples of varying impedance values. The instrument's testing and calibration processes are fully controlled via a mobile App. Once calibrated, the App autonomously selects the appropriate sampling resistor based on the characteristics of the rock sample during measurement, performs data calibration, and displays the processed data in real time on the software interface, demonstrating strong practicality.

The calibration method offers the following advantages:

- **Simplicity:** It eliminates the need to consider the size of the instrument's internal acquisition channel distributed capacitance separately; calibration can be performed solely on the results from the direct and reverse connection tests.
- **Detail:** The calibration content is refined, with the influence of the parasitic capacitance of the sampling resistor included in the equations, leading to a more comprehensive consideration.
- **High Precision:** The adaptive testing method can achieve a testing accuracy of 0.1% for high-impedance samples (above 1 M Ω), outperforming traditional small sampling resistor calibration methods.

Based on the design of two measurement devices, the measurement errors caused by device effects were re-analyzed, leading to further improvements in the calibration algorithm. Through extensive testing with multiple circuit models and actual samples, the accuracy of the calibration method was verified, demonstrating good performance in practical applications. The resistivity accuracy achieved is 1%, with phase accuracy below 0.1 mrad at frequencies below 10 kHz, and phase accuracy controlled within 2 mrad between 10 kHz and 100 kHz. Comparative testing with the Solartron 1260A impedance analyzer showed that the system and calibration method yield superior results for high-impedance samples. Additionally, tests with actual rock samples confirmed the effectiveness of the measurement system and calibration method in distinguishing mineralized samples, underscoring their significance for complex resistivity testing and rock physical property research.

On the other hand, the accuracy of the calibration method decreases as the test frequency increases. This decline is partly due to the lack of precise measurement of the stray impedances Z_1 and Z_4 between the power supply electrode and the receiving electrode. Related scholars have already conducted in-depth studies by altering the circuit design [28]. Additionally, electromagnetic coupling between the four-point measurement system increases rapidly with frequency, and it cannot be completely eliminated. Currently, a combined two-point and four-point testing approach is used to measure the complex resistivity of samples up to MHz frequencies, thereby further extending the frequency range of sample measurements [2].

Author Contributions: Conceptualization, R.C. and S.C.; methodology, R.C.; software, H.Z.; validation, H.Z. and C.X.; formal analysis, H.Z.; investigation, H.Z.; resources, C.X.; data acquisition and processing, H.Z.; writing—original draft preparation, H.Z.; writing—review and editing, R.C. and S.C.; supervision, R.C.; project administration, S.C.; funding acquisition, R.C. and S.C. All authors have read and agreed to the published version of the manuscript.

Funding: This research was funded by the National Key R&D Program of China (Grant No. 2022YFF0706201), the School-level Natural Science Research and Innovation Team Project (ZKTD202403), the Jiangsu Province Higher Education Basic Science (Natural Science) Research General Project (22KJB510044), the Jiangsu Province “Shuangchuang doctor” Program (JSSCBS20221066), the Jiangsu Province University Science and Technology Innovation Team Project.

Institutional Review Board Statement: Not applicable.

Informed Consent Statement: Not applicable.

Data Availability Statement: Data is contained within the article; further inquiries can be directed to the corresponding author.

Acknowledgments: This research greatly benefited from the generous support of Professor Lanfang He at the Institute of Geology and Geophysics, Chinese Academy of Sciences, who provided the Solartran 1260A impedance analyzer. We also sincerely thank Hongchun Yao and Ruijie Shen of Central South University for their invaluable insights and constructive suggestions.

Conflicts of Interest: The authors declare no conflicts of interest.

References

1. Kemna, A.; Binley, A.; Cassiani, G.; Niederleithinger, E.; Revil, A.; Slater, L.; Williams, K.H.; Orozco, A.F.; Haegel, F.H.; Hördt, A. An overview of the spectral induced polarization method for near-surface applications. *Near Surf. Geophys.* **2012**, *10*, 453–468. [[CrossRef](#)]
2. Vinegar, H.; Waxman, M. Induced polarization of shaly sands. *Geophysics* **1984**, *49*, 1267–1287. [[CrossRef](#)]
3. Pelton, W.H.; Ward, S.H.; Hallof, P.; Sill, W.; Nelson, P.H. Mineral discrimination and removal of inductive coupling with multifrequency IP. *Geophysics* **1978**, *43*, 588–609. [[CrossRef](#)]
4. Halisch, M.; Grelle, T.; Hupfer, S.; Blanke, J.-T.; Lehne, C. A new and modular laboratory core holder for high-precision measurements with low frequency impedance spectroscopy on natural rocks. In Proceedings of the International Symposium of the Society of Core Analysts (SCA), Vienna, Austria, 27 August–1 September 2017; p. SCA2017-069.
5. Revil, A.; Vaudelet, P.; Su, Z.; Chen, R. Induced polarization as a tool to assess mineral deposits: A review. *Minerals* **2022**, *12*, 571. [[CrossRef](#)]
6. Flores Orozco, A.; Aigner, L.; Gallistl, J. Investigation of cable effects in spectral induced polarization imaging at the field scale using multicore and coaxial cables. *Geophysics* **2021**, *86*, E59–E75. [[CrossRef](#)]
7. Gallistl, J.; Weigand, M.; Stumvoll, M.; Ottowitz, D.; Glade, T.; Orozco, A.F. Delineation of subsurface variability in clay-rich landslides through spectral induced polarization imaging and electromagnetic methods. *Eng. Geol.* **2018**, *245*, 292–308. [[CrossRef](#)]
8. Binley, A.; Hubbard, S.S.; Huisman, J.A.; Revil, A.; Robinson, D.A.; Singha, K.; Slater, L.D. The emergence of hydrogeophysics for improved understanding of subsurface processes over multiple scales. *Water Resour. Res.* **2015**, *51*, 3837–3866. [[CrossRef](#)]
9. Weller, A.; Börner, F. Measurements of spectral induced polarization for environmental purposes. *Environ. Geol.* **1996**, *27*, 329–334. [[CrossRef](#)]
10. Ragheb, T.; Geddes, L. The polarization impedance of common electrode metals operated at low current density. *Ann. Biomed. Eng.* **1991**, *19*, 151–163. [[CrossRef](#)]
11. Corona-Lopez, D.D.; Sommer, S.; Rolfe, S.A.; Podd, F.; Grieve, B.D. Electrical impedance tomography as a tool for phenotyping plant roots. *Plant Methods* **2019**, *15*, 49. [[CrossRef](#)]
12. Ehosioke, S.; Nguyen, F.; Rao, S.; Kremer, T.; Placencia-Gomez, E.; Huisman, J.A.; Kemna, A.; Javaux, M.; Garré, S. Sensing the electrical properties of roots: A review. *Vadose Zone J.* **2020**, *19*, e20082. [[CrossRef](#)]
13. Lesmes, D.P.; Morgan, F.D. Dielectric spectroscopy of sedimentary rocks. *J. Geophys. Res. Solid Earth* **2001**, *106*, 13329–13346. [[CrossRef](#)]
14. Revil, A. Spectral induced polarization of shaly sands: Influence of the electrical double layer. *Water Resour. Res.* **2012**, *48*, W02517. [[CrossRef](#)]
15. Zonge, K.L. Electrical Properties of Rocks as Applied to Geophysical Prospecting. Ph.D. Thesis, The University of Arizona, Tucson, AZ, USA, 1972.
16. Garcia, A.P.; Heidari, Z. A New Numerical Simulation Framework to Model the Electric Interfacial Polarization Effects and Corresponding Impacts on Complex Dielectric Permittivity Measurements in Sedimentary Rocks. *Math. Geosci.* **2024**, *56*, 1073–1103. [[CrossRef](#)]
17. Revil, A.; Skold, M. Salinity dependence of spectral induced polarization in sands and sandstones. *Geophys. J. Int.* **2011**, *187*, 813–824. [[CrossRef](#)]

18. Binley, A.; Slater, L.D.; Fukes, M.; Cassiani, G. Relationship between spectral induced polarization and hydraulic properties of saturated and unsaturated sandstone. *Water Resour. Res.* **2005**, *41*, W12417. [[CrossRef](#)]
19. Slater, L.; Lesmes, D.P. Electrical-hydraulic relationships observed for unconsolidated sediments. *Water Resour. Res.* **2002**, *38*, 1213. [[CrossRef](#)]
20. Peng, X.; Chun, S.; Su, B.; Chen, R.; Hou, S.; Xu, C.; Zhang, H. Design of Three-Dimensional Electrical Impedance Tomography System for Rock Samples. *Appl. Sci.* **2024**, *14*, 1671. [[CrossRef](#)]
21. Olhoeft, G. Low-frequency electrical properties. *Geophysics* **1985**, *50*, 2492–2503. [[CrossRef](#)]
22. Abdulsamad, F.; Florsch, N.; Schmutz, M.; Camerlynck, C. Assessing the high frequency behavior of non-polarizable electrodes for spectral induced polarization measurements. *J. Appl. Geophys.* **2016**, *135*, 449–455. [[CrossRef](#)]
23. Xin, Y.; Wang, Y.; Song, X.; Tong, J.; Hou, T.; Liu, H.; Cui, M. All solid-state electrode with low contact resistance and low polarization for measuring the electrical properties of rocks. *IEEE Trans. Instrum. Meas.* **2023**, *72*, 1008209. [[CrossRef](#)]
24. Charnock, D. Electromagnetic interference coupling between power cables and sensitive circuits. *IEEE Trans. Power Deliv.* **2005**, *20*, 668–673. [[CrossRef](#)]
25. Zimmermann, E.; Huisman, J.; Mester, A.; Van Waasen, S. Correction of phase errors due to leakage currents in wideband EIT field measurements on soil and sediments. *Meas. Sci. Technol.* **2019**, *30*, 084002. [[CrossRef](#)]
26. Zimmermann, E.; Huisman, J. The effect of heterogeneous contact impedances on complex resistivity measurements. *Geophys. J. Int.* **2024**, *236*, 1234–1245. [[CrossRef](#)]
27. Zimmermann, E.; Kemna, A.; Berwix, J.; Glaas, W.; Münch, H.; Huisman, J. A high-accuracy impedance spectrometer for measuring sediments with low polarizability. *Meas. Sci. Technol.* **2008**, *19*, 105603. [[CrossRef](#)]
28. Huisman, J.A.; Zimmermann, E.; Esser, O.; Haegel, F.-H.; Treichel, A.; Vereecken, H. Evaluation of a novel correction procedure to remove electrode impedance effects from broadband SIP measurements. *J. Appl. Geophys.* **2016**, *135*, 466–473. [[CrossRef](#)]
29. Wang, C.; Slater, L.D. Extending accurate spectral induced polarization measurements into the kHz range: Modelling and removal of errors from interactions between the parasitic capacitive coupling and the sample holder. *Geophys. J. Int.* **2019**, *218*, 895–912. [[CrossRef](#)]
30. Volkmann, J.; Klitzsch, N. Wideband impedance spectroscopy from 1 mHz to 10 MHz by combination of four-and two-electrode methods. *J. Appl. Geophys.* **2015**, *114*, 191–201. [[CrossRef](#)]
31. Wang, H.; Huisman, J.A.; Zimmermann, E.; Vereecken, H. Tackling capacitive coupling in broad-band spectral electrical impedance tomography (sEIT) measurements by selecting electrode configurations. *Geophys. J. Int.* **2024**, *238*, 187–198. [[CrossRef](#)]
32. Kemna, A.; Huisman, J.A.; Zimmermann, E.; Martin, R.; Zhao, Y.; Treichel, A.; Flores Orozco, A.; Fechner, T. Broadband electrical impedance tomography for subsurface characterization using improved corrections of electromagnetic coupling and spectral regularization. In *Tomography of the Earth's Crust: From Geophysical Sounding to Real-Time Monitoring*; Geotechnologien Science Report No. 21; Springer: Berlin/Heidelberg, Germany, 2014; pp. 1–20.
33. He, Z.; Cai, H.; Li, S.; Xian, J.; Hu, X. Extracting IP parameters of rock samples using machine learning. *Geophys. J. Int.* **2023**, *235*, 862–878. [[CrossRef](#)]
34. Wang, H.; Huisman, J.A.; Zimmermann, E.; Vereecken, H. Experimental design to reduce inductive coupling in spectral electrical impedance tomography (sEIT) measurements. *Geophys. J. Int.* **2021**, *225*, 222–235. [[CrossRef](#)]
35. CHENG, H.; FU, S.; LI, D.; CUI, J.; LIAO, X.; FU, G. Research on acquisition method of rock and ore electrical parameters based on IRmPRBS. *Prog. Geophys.* **2022**, *37*, 374–385.
36. Guo, C.; Liu, R.; Chen, X.; Mavko, G.; He, Z. An ultra-wideband measurement method for the dielectric property of rocks. *IEEE Geosci. Remote Sens. Lett.* **2019**, *16*, 874–878. [[CrossRef](#)]
37. Gurin, G.; Fomina, E.; Emelianov, V.; Kozlov, E. New equipment for high-accuracy laboratory measurements of spectral induced polarization of rock samples in the time-and frequency domains: Testing of laboratory multifunction potentiostat-galvanostat. *J. Appl. Geophys.* **2022**, *203*, 104703. [[CrossRef](#)]
38. Vanhala, H.; Soinenen, H. Laboratory technique for measurement of spectral induced polarization response of soil samples. *Geophys. Prospect.* **1995**, *43*, 655–676. [[CrossRef](#)]

Disclaimer/Publisher's Note: The statements, opinions and data contained in all publications are solely those of the individual author(s) and contributor(s) and not of MDPI and/or the editor(s). MDPI and/or the editor(s) disclaim responsibility for any injury to people or property resulting from any ideas, methods, instructions or products referred to in the content.